Published in final edited form as:
Eur J Pharm Biopharm. 2013 September ; 85(1): 119–129. doi:10.1016/j.ejpb.2013.02.011.

Remodeling of tissue-engineered bone structures *in vivo*

Sandra Hofmann[a,*], **Monika Hilbe**[b], **Robert J. Fajardo**[c], **Henri Hagenmüller**[d], **Katja Nuss**[e], **Margarete Arras**[f], **Ralph Müller**[d], **Brigitte von Rechenberg**[e], **David L. Kaplan**[g], **Hans P. Merkle**[a], and **Lorenz Meinel**[a,g]

Sandra Hofmann: sahofmann@ethz.ch; Monika Hilbe: hilbe@vetpath.uzh.ch; Robert J. Fajardo: fajardor@uthscsa.edu; Henri Hagenmüller: henri.hagenmueller@gmail.com; Katja Nuss: katja.nuss@vetclinics.uzh.ch; Margarete Arras: margarete.arras@uzh.ch; Ralph Müller: ram@ethz.ch; Brigitte von Rechenberg: bvonrechenberg@vetclinics.uzh.ch; David L. Kaplan: David.Kaplan@tufts.edu; Hans P. Merkle: hmerkle@pharma.ethz.ch; Lorenz Meinel: lorenz.meinel@pharmazie.uni-wuerzburg.de

[a]Institute of Pharmaceutical Sciences, ETH Zurich, Zurich, Switzerland [b]Institute of Veterinary Pathology, Vetsuisse Faculty, University of Zurich, Zurich, Switzerland [c]Orthopaedic Biomechanics Laboratory, Beth Israel Deaconess Medical Center, Harvard Medical School, Boston MA [d]Institute for Biomedical Engineering, University and ETH Zurich, Zurich, Switzerland [e]Musculoskeletal Research Unit (MSRU), Center for Applied Biotechnology and Molecular Medicine (CABMM), Faculty of Veterinary Medicine, University of Zurich, Switzerland [f]University Hospital Zurich and Institute of Laboratory Animal Science, Vetsuisse Faculty, University of Zurich, Zurich, Switzerland [g]Department of Biomedical Engineering, Tufts University, Medford, MA

Abstract

Implant design for bone regeneration is expected to be optimized when implant structures resemble the anatomical situation of the defect site. We tested the validity of this hypothesis by exploring the feasibility of generating different *in vitro* engineered bone-like structures originating from porous silk fibroin scaffolds decorated with RGD sequences (SF-RGD), seeded with human mesenchymal stem cells (hMSC). Scaffolds with small (106 – 212 μm), medium (212 – 300 μm) and large pore diameter ranges (300 – 425 μm) were seeded with hMSC and subsequently differentiated *in vitro* into bone-like tissue resembling initial scaffold geometries and featuring bone-like structures. Eight weeks after implantation into calvarial defects in mice, the *in vitro* engineered bone-like tissues had remodeled into bone featuring different proportions of woven/lamellar bone bridging the defects. Regardless of pore diameter all implants integrated well, vascularization was advanced and, bone marrow ingrowth had started. Ultimately, in this defect model, the geometry of the *in vitro* generated tissue-engineered bone structure, trabecular- or plate-like, had no significant impact on the healing of the defect, owing to an efficient remodeling of its structure after implantation.

[*]Please direct correspondence to: ETH Zurich, Dr. Sandra Hofmann, Institute for Biomechanics, HPI F26, Wolfgang-Pauli-Str. 10, CH-8093 Zurich, Switzerland, tel.: +41 44 633 70 82, fax: +41 44 633 15 73, sahofmann@ethz.ch.

Conflict of interest
The Authors declare that they have no conflicts of interest to disclose.

Disclosure
No disclosure.

Keywords

Remodeling; tissue engineering; bone; in vivo; stem cell; silk-fibroin

1. Background

The reconstruction of large bone segments remains a clinical need and none of the current approaches is ideal. All have fundamental drawbacks, such as difficulties in shaping the graft, the lack of sufficient filling material, potential risk of cell-mediated immune responses to alloantigens, transmission of pathogens and infections [1–6]. The goal of a successful bone tissue graft is to restore the anatomical, physiological and functional status of the tissue. Restoration must also compensate for a possible deficiency in the number or function of local connective tissue progenitors, as may occur in regions of previous trauma, infection, prior irradiation, tissue defects, scar tissue, or compromised vascularity [7–10]. Although many of the underlying regenerative mechanisms still need to be addressed, tissue-engineered bone grafts have the potential to address these points [11–13].

Silk fibroin (SF) from the silkworm *Bombyx mori L.* and its decoration with covalently bound, cell adhesive RGD sequences has become a biocompatible option as a biomimetic scaffold for the *in vitro* engineering of bone, cartilage and ligaments [14–19]. For bone regeneration, slowly degrading biomaterials maintaining implant integrity following implantation while continually transferring the load-bearing burden to the developing and functional host tissue are considered ideal [20–22]. Many natural and synthetic biomaterials have been explored for load-bearing applications *in vivo*. Rapidly degrading polymers such as collagen and some synthetic polyesters have been shown to transfer load-bearing function to developing tissue prior to sufficient ingrowth and remodeling, resulting in mechanical failure of the graft [23, 24]. In contrast, non-degradable materials such as polytetrafluorethylene, polyester, carbon fiber and polypropylene failed to support host tissue ingrowth and remodeling, a finding suggested to be a result of stress shielding in high load-bearing applications [25]. SF has been shown to be biodegradable *in vivo* within a time frame of one to two years, and is known to have good load-bearing capacity [14, 25–27].

The literature contains several studies that link scaffold geometries to tissue-engineered morphologies [21, 28–30] and to vascularization processes and bone ingrowth *in vivo* [30–33]. However, the present study is to our knowledge the first that reports on the remodeling of diverse *in vitro* tissue-engineered bone structures on SF-RGD scaffolds with different pore diameter ranges after implantation into a critical sized cranial defect in mice. Furthermore, our work explores the influence of tissue-engineered bone morphology generated *in vitro* on implant success *in vivo* and tracks the associated healing events.

2. Materials and methods

2.1. Materials

Fetal bovine serum (FBS), RPMI 1640 medium, Dulbecco's Modified Eagle Medium (DMEM), basic fibroblast growth factor (bFGF), transforming growth factor-β1 (TGF- β1), penicillin and streptomycin (Pen-Strep), Fungizone, nonessential amino acids (NEAA, consisting of 8.9 mg/L L-alanine, 13.21 mg/L L-asparagine, 13.3 mg/L L-aspartic acid, 14.7 mg/L L-glutamic acid, 7.5 mg/L glycine, 11.5 mg/L L-proline, 10.5 mg/L L serine), and trypsin were from Gibco (Carlsbad, CA). Ascorbic acid-2-phosphate, dexamethasone, β-glycerophosphate and glycine-arginine-alanine-aspartate-serine (GRGDS) peptide were from Sigma (St. Louis, MO). 1-Ethyl-3-(dimethylaminopropyl) carbodiimide hydrochloride (EDC) and N-hydroxy-succinimide (NHS) were purchased from Pierce (Rockford, IL). All

other substances were of analytical or pharmaceutical grade and obtained from Sigma. Silkworm cocoons were kindly supplied by M. Tsukada (Institute of Sericulture, Tsukuba, Japan). Bone morphogenic protein 2 (BMP-2) was kindly provided by Wyeth Biopharmaceuticals (Andover, MA).

2.2. Scaffold preparation

SF-RGD scaffolds were prepared as described previously [34, 35]. In brief, cocoons from *B. mori* were boiled for 1 hour in an aqueous solution of 0.02M Na_2CO_3 and rinsed with water to extract sericins. Purified silk was solubilized in 9M LiBr solution and dialyzed (Pierce, MWCO 3500 g/mol) first against water for 1 day and then against 0.1M 2-(N-morpholino)ethanesulfonic acid buffer (MES), 0.5M NaCl, pH 6, for 1 day. For conjugation with RGD sequences, SF solution was coupled with GRGDS peptide as previously described [34]. Briefly, the carboxyl groups on SF were first activated by reaction with EDC/NHS for 15 min at room temperature. To quench excessive EDC, 70 μl/ml β-mercaptoethanol was added. The solution was then incubated with 0.5 g/l peptide for 2 h at room temperature. The reaction was stopped with 10 mM hydroxylamine. Purified SF-RGD was dialyzed against 0.1 M MES, pH 4.5–5, for 1 day, lyophilized and redissolved in hexafluoro-2-propanol (HFIP) to obtain a 17% (w/v) solution. Granular NaCl crystals were used as porogen. Sieved fractions in the range of small (106–212 μm), medium (212–300 μm) or large (300–425 μm) diameters were weighed into a Teflon container and SF-RGD/HFIP solution was added at a ratio of 20:1 (NaCl/SF-RGD). HFIP was allowed to evaporate for 2 days and NaCl/SF-RGD blocks were immersed in 90% (v/v) methanol for 30 minutes to induce a conformational transition to β-sheet [34]. Blocks were removed, dried and NaCl was extracted by incubation in water for 2 days, resulting in scaffolds with >90% porosity [34]. Disk shaped scaffolds (8 mm diameter, 2 mm thick) were prepared using a dermal punch (Miltey, Lake Success, NY), and steam autoclaved at 121°C for 15 min.

2.3. Scanning electron microscopy (SEM)

The microstructure of dry and platinum-coated SF-RGD scaffolds was characterized using scanning electron microscopy (SEM, Zeiss Leo Gemini 1530; Oberkochen, Germany) at a voltage of 5 kV.

2.4. Cell isolation, expansion and characterization

Human mesenchymal stem cells (hMSC) were isolated by cell adhesion to tissue culture plastic from 25 cm^3 whole bone marrow obtained from Clonetics (Santa Rosa, CA). Five-ml aliquots of bone marrow were diluted in 100 ml of *isolation medium* (RPMI 1640 supplemented with 5% FBS). Cells were pelleted, resuspended in *expansion medium* (DMEM, 10% FBS, Pen-Strep, Fungizone, NEAA and 1 ng/ml bFGF) and seeded in 175 cm^2 flasks at a density of 5×10^4 cells/cm^2. The adherent cells were allowed to reach approximately 80% confluence (12–17 days for the first passage). Cells were trypsinized and replated every 6–8 days at approximately 80% confluence. Second passage (P2) cells were used if not otherwise stated. To assess the mesenchymal character of the cells, they were characterized prior to use with respect to: (a) the expression of surface antigens and (b) the ability to selectively differentiate into the chondrogenic or osteogenic lineage in response to environmental stimuli, as previously described [36–38].

2.5. Tissue culture in vitro

Per scaffold, 5×10^6 hMSC were suspended in 20 μl liquid BD Matrigel Basement Membrane Matrix (BD Biosciences, San Jose, CA. The cell suspension was seeded onto prewetted scaffolds and placed in an incubator (37°C, 5% CO_2) for 15 min to allow gel hardening. For cultivation in spinner flasks, the cell-seeded SF-RGD scaffolds were

threaded onto 4 needles embedded in the stoppers of the spinner flask (2 scaffolds per needle) [28]. Flasks were filled with 150 ml *control* (DMEM, 10% FBS, Pen-Strep, Fungizone) or *osteogenic medium* (control medium supplemented with 50 μg/ml ascorbic acid-2-phosphate, 10 nM dexamethasone, 10 mM β-glycerophosphate) and 1 μg/ml bone morphogenetic protein-2 and placed in a humidified incubator (37°C, 5% CO_2), with the side arm caps loosened to permit gas exchange, and stirred with a magnetic bar at 60 min^{-1}. Half the medium was replaced 3 times a week for 5 weeks of cultivation. For *in vivo* implantation, the tissue-engineered constructs were punched with a dermal punch (Miltey, Lake Success, NY), into disks (5 mm diameter, 2 mm thick).

2.6. Characterization of constructs before implantation

2.6.1. Calcium deposition—After 5 weeks of cultivation in bioreactors, scaffolds were blotted on a clean paper towel and their wet weight was noted. After cutting into two halves, the scaffolds (n=5) were weighed again and disintegrated using steel balls and a Minibead-beater (Biospec, Bartlesville, OK) in 1 ml 5% trichloroacetic acid in water. After a second extraction with 1 ml 5% trichloroacetic acid in water for 30 minutes and combination of the samples, calcium content was measured spectrophotometrically at 575 nm using *o*-cresolphthalein complexone according to the manufacturer's protocol (Sigma, St. Louis, MO).

2.6.2. Micro-computed tomography (μCT)—Constructs were analyzed by μCT on a μCT 20 imaging system (Scanco Medical, Brüttisellen, Switzerland) providing an isotropic resolution of 34 μm. A constrained Gaussian filter was used to partly suppress noise. Mineralized tissue was segmented from non-mineralized tissue using a global thresholding procedure [39]. A single global threshold was visually determined and applied to all samples to evaluate their structural differences. All samples were thresholded by using the same filter width (1.2), filter support (1). Quantitative morphometry was performed to assess bone volume (BV), bone surface per total volume (BS/TV), bone surface-to-volume ratio (BS/BV), trabecular thickness (Tb.Th), and trabecular number (Tb.N) using direct microstructural bone analysis [40]. Three-dimensional visualizations were generated using in-house software [41]. Constructs used for micro-structural assessment before implantation were not implanted into animals due to sterility issues.

2.7. Animals and housing procedure

Twelve female BALB/cOlaHsd-Foxn1nu mice were obtained from a commercial supplier (Harlan, Horst, Netherlands) at the age of six weeks with body weights ranging from 18 to 21 g. All mice were free of viral, bacterial, and parasitic pathogens listed in the recommendations of the Federation of European Laboratory Animal Science Associations. After an adaptation period of two weeks, surgery was performed and constructs were implanted. The animals' health status was monitored by a sentinel program throughout the experiment. They were kept in groups of six in type three individually ventilated cages with dust-free wooden bedding and paper towels as nesting material. They were fed a pelleted mouse diet (Kliba No. 3431, Provimi Kliba, Kaiseraugst, Switzerland) *ad libitum*, and had free access to sterilized drinking water. The light/dark cycle in the room consisted of 12/12 h of artificial light. The climate was 21±1°C, with a relative humidity of 50±5%, and with 15 complete changes of filtered air per hour. Housing and experimental procedures were in accordance with the Swiss animal protection law and conformed to the European Convention for the protection of vertebrate animals used for experimental and other scientific purposes (Council of Europe nr.123 Strasbourg 1985). All experimental procedures were approved by the local laboratory animal care and use committee (Kantonales Veterinäramt Zürich, Zürich, Switzerland).

2.8. Mouse calvarial defect model - surgery

Mice (n=12) were anesthetized by inhalation of isoflurane (Isoflo, Abbott, Baar, Switzerland) in a concentration of 2–3% in 100% oxygen at a flow rate of 200 ml/min through a nose mask. Ketamine (Ketasol-100™, Dr. Graub, Bern, Switzerland) was injected subcutaneously as pre-medication at a dosage of 40 mg/kg body weight for pre-emptive analgesia. After fixing the head with the help of an assisting person, the skin above the cranium was incised with a scalpel, retracted with a skin retractor and the periosteum removed. Then two defects of 4 mm in diameter were drilled with a dental drill carefully avoiding dural perforation. The remaining inner bone layer was cautiously removed by Pean forceps. The surgical area was flushed with sterile saline to remove bone debris. The two defects per mouse were randomly assigned to one of four treatment groups receiving either pre-differentiated hMSC on SF-RGD scaffolds with either small (106–112 μm), medium (212–300 μm) or large (300–425 μm) pore diameters. A forth group served as a control with defects left empty. Skin was closed by interrupted single layer sutures with Polyglactin 6-0 (Vicryl™, Johnson&Johnson Intl., Brussels, Belgium). Post-operative pain was treated with buprenorphine (Temgesic™, Reckitt and Colman Products Ltd., Hull, England) at a dose of 0.1 mg/kg body weight and injected subcutaneously twice per day for 3 days. Mice were sacrificed after 8 weeks with CO_2 asphyxiation, the skull was explanted in toto after removing the skin, lower jaw and cervical vertebrae by surgical scissors and put into 10% neutral buffered formaline at 4°C for 48 h for tomographical and histological analysis.

2.9. Post mortem μCT

Calvarial explants were analyzed by μCT on a μCT 40 imaging system (Scanco Medical, Brüttisellen, Switzerland) providing an isotropic resolution of 30 μm. A constrained Gaussian filter was used to partly suppress noise. Mineralized tissue was segmented from non-mineralized tissue using a global thresholding procedure [39]. All samples were thresholded by using the same filter width (1.2), filter support (1). For morphometrical analysis, the defect volume was chosen visually by fitting a disk of 4 mm in diameter into the respective defect locations. Quantitative morphometry and three-dimensional visualization were performed as described in paragraph 2.6.2.

2.10. Post-mortem histology

Formalin-fixed (4%) and decalcified (12% EDTA, pH 7.0) calvarial explants were dehydrated in graded ethanol solutions and xylene and cross-sectioned in the center as most deficits concerning bone ingrowth and resorption were supposed to be found there. After embedding in paraffin, the explants were cut into 3 μm thick sections and stained with H&E. Qualitative assessments were followed by a semiquantitative analysis using a score system. Scaffold areas were divided into caudal, medial and apical regions and scored for new bone formation (score 0%, 1–10%, 11–25%, 26–50% and >50%), vascularization (0 for none, 1 for few, 2 for moderate, 3 for many), amount of fibrous tissue (0 for none, 1 for few, 2 for moderate, 3 for a lot), foreign body reaction (macrophages and foreign body cells together: 0 for none, 1 for few, 2 for moderate, 3 for many), and inflammatory parameters such as lymphocytes (0 for none, 1 for few, 2 for moderate, 3 for many) and neutrophil granulocytes (0 for none, 1 for few, 2 for moderate, 3 for many).

2.11. Statistical analysis

Statistical analysis was performed using SPSS software (SPSS Inc., Chicago, IL). The influence of scaffold pore diameter on morphometric and biochemical parameters was analyzed using one-way ANOVA and Fisher's least significant difference posthoc analysis at a 95% confidence level. Semiquantitative histological data were subjected to a

generalized linear model approach. Data are expressed as mean values ± standard deviations and results were considered to be significant at $p < 0.05$ and highly significant at $p < 0.01$.

3. Results

3.1. In vitro osteogenesis

SF-RGD scaffold appearance and pore diameter were imaged using SEM (Figure 1A-C). Pore diameters of the scaffolds corresponded with the chosen porogen diameters during manufacture, yielding small (106–212 μm; Figure 1A), medium (212–300 μm; Figure 1B) and large pores (300–425 μm; Figure 1C), respectively. hMSC seeded SF-RGD scaffolds cultured in spinner flasks under osteogenic conditions for 5 weeks were analyzed for osteogenic differentiation and cell proliferation. μCT imaging demonstrated that the SF-RGD structure acted as a template for the deposition of mineralized extracellular matrix by the differentiating cells. This allowed guiding the formation of bone-like structures leading to small (Figure 1D, 1G, 1J), medium (Figure 1E, 1H, 1K) and large (Figure 1F, 1I, 1L) features which were found throughout the scaffold volume. More bone-like structure was deposited at the perimeter of the scaffolds when compared to the center. Magnifications showed more rodlike geometries in the presence of medium and large pores (Figure 1K, 1L), while scaffolds with small pores exhibited more plate-like structures that were formed along the scaffold boundaries (Figure 1J). Quantitative μCT analysis (mean ± standard deviation) showed a significant difference in BV for the large pores ($11.56 \pm 4.0\ mm^3$) when compared to medium pores ($5.68 \pm 3.0\ mm^3$; $p < 0.01$) and small pores ($7.36 \pm 3.3\ mm^3$; $p < 0.05$, Figure 2A). BS/TV was $3.21 \pm 1.1\ mm^{-1}$, $2.79 \pm 1.4\ mm^{-1}$, and $4.37 \pm 1.4\ mm^{-1}$ for small, medium and large pores, respectively, with a statistical difference between medium and large pore diameters ($p < 0.05$, Figure 2B). BS/BV showed significant differences between small and large pores (45.5 ± 6 and 38.4 ± 3, respectively; $p < 0.05$) and between medium and large pores (50.1 ± 6 and 38.4 ± 3, respectively; $p < 0.001$, Figure 3C). Tb.Th increased with increasing scaffold pore diameters, with an average thickness of 0.071 ± 0.01 mm, 0.074 ± 0.02 mm and 0.088 ± 0.01 mm for small, medium and large pores, respectively (Figure 3D). Statistically, a significant difference between small and large pores ($p < 0.005$) and medium and large pores was observed ($p < 0.05$). Similarly, the number of trabeculae per length increased with increasing pore diameter of the scaffold, with values of 0.962 ± 0.22, 1.273 ± 0.30 and 1.505 ± 0.12 for small, medium and large pores, respectively (Figure 3E), and significant differences between small and medium pores and small and large pores ($p < 0.05$ and $p < 0.0005$, respectively).

Calcium deposition per mg scaffold wet weight (mean ± standard deviation) was 8.2 ± 1.2 μg for scaffolds with small pores, 10.9 ± 3.9 μg with medium pores and 12.3 ± 6.1 μg with large pores. In spite of a trend for more calcium deposition with larger pore diameter scaffolds the differences were not statistically significant, (Figure 3A). The relationship between DNA per mg scaffold as a measure of cell number and scaffold pore diameter was inverse but without statistical significance as analyzed by one-way ANOVA (Figure 3B). For all scaffold pore diameter ranges histology showed a regular distribution of cells throughout the scaffolds using H&E staining (Figure 3C, 3D, 3E). Von Kossa staining for mineralized tissue was positive around cells and on the scaffold surface, exclusively for cells grown in osteogenic medium (Figure 3F, 3G, 3H), but negative for cells grown in control medium (data not shown).

3.2. In vivo osteogenesis

Surgery was performed without complications and all mice recovered well. One mouse showed microscopic signs of neutrophilic or suppurative inflammation, which was attributed to a skin infection and resulted in ulceration and necrosis of the skin and affected the

underlying tissues. This mouse was disregarded for further evaluation. Eight weeks after surgery, the animals were sacrificed and the morphology of the formed bone was analyzed using μCT (Figure 4). Without implants, defects showed little evidence of bone formation (Figure 4A, 4B, 4C), whereas defects with implanted tissue-engineered constructs showed filling with considerable amounts of bone-like structures (Figure 4). The constructs used for this study were thicker than the defect resulting in an overhang of the scaffolds above the host bone. Quantitative μCT analysis (mean ± standard deviation) showed no difference between the three different pore diameters of the underlying scaffolds for BV and BS/TV. Bone volume was 13.80 ± 3 mm^3, 10.56 ± 3 mm^3 and 11.51 ± 3 mm^3, for small, medium or large pore diameters of the scaffolds, respectively (Figure 5A), while bone surface per total volume was 4.52 ± 1.1 mm^{-1}, 4.99 ± 0.9 mm^{-1} and 4.32 ± 1.6 mm^2 (Figure 5B). The resulting BS/BV showed significant differences between small and medium pores (8.3 ± 1 and 12.3 ± 2, and $p < 0.005$) and between medium and large pores (12.3 ± 2 and 9 ± 1; $p < 0.05$, Figure 5C). Tb.Th showed values of 0.327 ± 0.03 mm, 0.232 ± 0.01 mm and 0.281 ± 0.03 mm for small, medium and large pores, respectively (Figure 5D). Statistically, there was a significant difference between small and medium pores ($p < 0.005$) and medium and large pores ($p < 0.05$). Tb.N increased with increasing pore diameter, with values of 1.496 ± 0.32, 1.866 ± 0.24 and 1.980 ± 0.08 for small, medium and large pores, respectively (Figure 5E), with significant differences between small and large pores ($p = 0.034$).

Histological evaluations corroborated the findings made by μCT (Figure 6, Figure 7). Empty defects showed normal skin growth and very little new bone formation at the borders of the defect with no conspicuous inflammation or foreign body reaction (Figure 6A). The implants were well integrated to the extent that host bone was difficult to differentiate from new bone. Foreign body and inflammatory reactions were in a range expected for such a defect, showing variable amounts of macrophages and foreign body cells as well as lymphocytes and neutrophil granulocytes [42, 43]. Implants showed normal bone growth and vascularization, as well as bone marrow ingrowth together with new bone formation (Figure 7A). Newly formed bone consisted to a large part of mature lamellar bone, although polarized light evidenced that collagen bundles were not as dense as in mature bone and sometimes showed thick fibers, as expected for woven bone (data not shown). The healing of defects treated with tissue-engineered implants was characterized through caudal and apical layers of new bone, whereas in the center of the implant, fibrous tissue was found along with clusters of new bone (Figure 6B–D), as demonstrated by separate semiquantitative evaluation of the apical and caudal part of the implant and its central part (Figure 8). New bone formation did not depend on implant pore diameter or on scaffold vascularization. Throughout the implant, but particularly in the central part and for all pore diameters, clusters of beginning mineralization were found in void pores of the constructs (Figure 7B). All implants were well vascularized, with the larger pores showing a tendency towards higher vascularization, although this trend was not statistically significant. Loose fibrous tissue was present in all implants to a similar extent. As above, the foreign body reaction in reponse to the constructs was within expected range, with some macrophages and foreign body giant cells. Foreign body reactions were particularly situated at the rims of the SF-RGD scaffold that showed an onset of mineralization (Figure 7C), with a slight tendency of the cells to accumulate on the apical side of the implant. Moderate numbers of lymphocytes were detected in all implants, their quantity decreasing with increasing pore diameters. Neutrophil granulocytes showed a similar tendency, and were more prominent than lymphocytes. The number of lymphocytes and neutrophils did not correlate with the degree of vascularization.

4. Discussion

Morphological as well as mechanical specifications for the design of implants for bone regeneration should be based on the anatomical conditions and requirements at the defect site. To mimic such anatomical features, we aimed at engineering different bone-like structures *in vitro* using SF-RGD scaffolds with different pore diameter ranges as blueprints for extracellular matrix deposition. Thereafter, the impact of different bone-like tissue structures on the subsequent bone healing process *in vivo* was evaluated in a critical-sized cranial defect in mice. The *in vitro* culture of hMSC on SF-RGD scaffolds in osteogenic medium using spinner flask bioreactors resulted in the formation of bone-like structures whose outcome was highly analogous to inorganic and organic components of physiological bone as has been determined by biochemical assays, and in earlier studies with X-ray diffractometry and RT-PCR [37, 38, 44]. While keeping the porosity of the SF-RGD scaffolds fairly constant (> 90%), we found the structure of the deposited bone-like tissue after five weeks in culture to depend largely on the pore diameter of the applied scaffold. This was demonstrated visually (Figure 1), morphometrically (Figure 2) and histologically (Figure 3). The *in vitro* engineering of bone-like structures on scaffolds with pore diameters larger than 200 μm resulted in interconnected rod-like structures with bone-like features. In contrast, on scaffolds with smaller pore diameters, bone-like structures concentrated at the periphery of the scaffold and adjacent bone-like structures exhibited coalescence of the fine trabeculae and resulted in the formation of more plate-like structures. Large pores resulted in the highest bone volume and calcium deposition, likely because the more open structure facilitated cell penetration and nutrient supply into the scaffold, which in turn resulted in better mass transport to and from the cells as well as better nutrient/metabolite exchange and enhanced cellular differentiation activity, as has been shown previously for other scaffold materials [37]. The possibility of engineering different bone-like structures might be particularly interesting for the subchondral bone plate, present at the interface between epiphysis and overlying hyaline cartilage in the transition zone between cortical and trabecular bone, so that implants are able to bear load and at the same time match patient and defect site structures [45].

Previous studies have shown that SF scaffolds without cells or with undifferentiated hMSC showed insufficient cell differentiation or recruitment of host cells for substantial *in vivo* healing of critical sized calvarial [46] or femoral defects [47, 48]. The experimental outcomes were comparable or better as those achieved with established scaffold materials like poly-caprolactone [49], polyglycolic acid scaffolds [50] and polyglycolic-polylactic acid [51]. In this study, the effect of constructs exhibiting differing tissue-engineered mineralized structures was assessed in a standard rodent *in vivo* model for bone regeneration. Progress in the repair of the defects was evaluated with respect to the effects different geometries of the *in vitro* engineered tissue had on defect repair *in vivo*. In fact, implantation resulted in enhanced bone regeneration and good biocompatibility of the tissue-engineered implants, whereas no substantial healing was visible in control defects. Some animals showed indications for minor implant migration off the inital placement; nonetheless, the final integration of the respective implants was equally effective. This outcome may be explained by the thickness of the implants, which markedly exceeded that of the cranium, and possibly because implants were fixed by a skin flap only not to confound bone repair and integration. Bone marrow ingrowth was well advanced at the outer rims of the implants and more pronounced in stronger mineralized parts; however, it was impossible to distinguish between the contributions of transplanted cells versus host cells. The increase in the extracellular matrix volume produced by those cells is expected to lower the porosity to such an extent that further growth is limited until vascularization of the tissue occurs [52, 53]. It corroborated with the decrease in the bone surface-to-volume ratio *in vivo* by a factor of approximately five, which was attributed to compaction of bone and

trabecular merging. Trabecular thickness was more than three-fold above that right after *in vitro* culture and no longer dependent on the pore diameter of the underlying scaffold. This reflects the onset of a remodeling of the tissue-engineered trabeculae into cortical bone following implantation. The advance in trabecular coalescence was in analogy to that previoulsy found with metaphyseal bone formation [54]. Obviously, different structures of *in vitro* engineered bone-like tissue converged after *in vivo* implantation and approached a structure independent of the underlying scaffold, which is in agreement with the recent postulate of Bohner et al. [55]. We hypothesize the final mineralized tissue morphology within the implant volume was largely guided by the adjacent native host bone. In those locations where the tissue-engineered structure did not fulfill the local needs, it was remodelled into the desired structure irrespective of a given scaffold pore diameter or prior *in vitro* engineered bone-like structure. To raise evidence that host bone structures guide the remodeling of pre-engineered bone structures into geometries resembling the adjacent uncompromised tissue further studies in preferentially cancellous bone regions need to be performed.

Histology served as a tool to ascertain general trends in biomaterial-tissue interactions and was used to evaluate the *in vivo* competence of our implants. Ratings were done semiquantitatively and did not show statistically significant differences between the three scaffold pore diameters or their influence on any of the parameters subjected to statistical analysis. This may result from the small numbers of animals and the intrinsic variability of biological responses, especially when the surgical procedure is demanding. Nevertheless, trends could be observed. The newly formed bone was irregularly distributed throughout the scaffold, with a layer of bone-like tissue on both the apical and the caudal side of the implant, whereas bone formation was less pronounced in the center. This is analogous to the calvarial bone plate, where apical and caudal sites are more compact than the middle zone.

The challenge of tissue-engineered implants is their fast vascularization after implantation in order to avoid necrosis in the implant's central parts [4, 10]. Previous studies have shown that while vascularized fresh bone grafts undergo excellent integration, non-vascularized (dead) bone does not integrate well with adjacent (living) bone, demonstrating the importance of vascularization for bone ingrowth and remodeling [10, 32, 56]. Prompt revascularization has also been shown to favor osteoblastic differentiation, whereas prolonged hypoxia caused formation of cartilage or fibrous tissue [10, 57, 58].

A trend towards better vascularization was observed for medium- and large-diameter pores versus small pores. More blood vessels were found on the apical sides of the implants, where histological evidence suggested further sprouting (Figure 8B). It can be speculated that the plate-like bone structures on implants with small pores or the scaffold itself hindered blood vessel ingrowth to some extent, a fact that might be corroborated with the higher variations in bone formation in these implants [59]. Fibrous tissue was to a large extent restricted to the central part of the scaffolds where bone growth was less advanced. Cell clusters located within pores showed signs of early mineralization (Figure 7B). They consisted of a mix of fibroblasts and cells that were considered to be hypertrophic chondrocytes. This raises evidence for endochondral ossification processes in restricted locations, which is normally not the case for calvarial defects, where intramembraneous bone formation is the natural process [60]. This effect is analogous to a previous study showing that relatively large pores allowed ready vascularization and direct osteogenesis, while smaller pores occasionally led to bone-like tissue via endochondral ossification [61].

Previous studies have demonstrated the excellent biocompatibility of purified SF [14, 62]. In our study, SF scaffolds decorated with RGD sequences and implanted *in vivo* showed a slight inflammatory response (lymphocytes and neutrophil granulocytes) and a moderate

foreign body reaction (macrophages and foreign-body giant cells), especially on the apical sides of the implants. The number of inflammatory cells decreased with increasing pore diameters of the underlying scaffold, with the larger void areas possibly facilitating vascularization, being favorable to restrict incidence and intensity of adverse tissue effects. Considering the mouse strain used in our study as well as the defect size, the observed inflammatory responses were considered in the range typical for a slowly degrading biomaterial as previously reported [63].

Our study raises the question whether one of the implanted morphologies would have favored earlier onset of *in vivo* regeneration. To answer this, earlier timepoints of animal sacrifice would be needed. After eight weeks the degradation of the implanted scaffolds was still minor, and only slightly enhanced in areas with high numbers of foreign body cells. It is anticipated that through sustained degradation the SF-RGD scaffold will slowly open new space for bone matrix deposition, and will be replaced through physiological bone turnover within one to two years [14, 25, 52]. A limitation of this study is that variable scaffold pore sizes at a constant porosity automatically affect the scaffold's mechanical properties, which have been shown to be potent regulators of cell function and tissue morphogenesis [64]. It needs to be taken into account that whenever this study allocates an effect to a certain pore diameter it might be as well be the result of different mechanical properties or different scaffold hydration that resulted from varying pore diameters.

In conclusion this study demonstrates that SF biomaterials allow tissue formation on the scaffold surface, while providing sufficient mechanical support, *in vitro* as well as in a non-load-bearing defect *in vivo.* Porous SF scaffolds decorated with RGD sequences provide a blueprint for the desired *in vitro* structure of bone-like tissue through the design of different scaffold geometries. In fact, by applying appropriate technology, the engineering of trabecular structures *in vitro* appears to be feasible. In case of a cranial or related defect in this mouse model, the structure of an *in vitro* cultured implant, once implanted, will be subject to remodeling and result in similar tissue outcomes independent of the previously engineered bone-like tissue, a result which is likely to be directed by the native bone environment. In the future, critical sized defects in predominately cancellous bone as well as in load-bearing areas will be investigated to test the utility of structurally tailored implants for tissue regeneration, host integration and functionality.

Acknowledgments

We thank Sandra Hanses for her assistance with surgery, and Flora Nicholls for managing anaesthesia, postoperative care and monitoring of the animals. Financial support by the Alexander von Humboldt Foundation (Bonn, Germany), NIH (P41 EB002520) the NCCR CO-ME of the Swiss National Science Foundation and ETH Zurich (TH-Gesuch) is gratefully acknowledged.

References

1. Salgado AJ, Coutinho OP, Reis RL. Bone tissue engineering: state of the art and future trends. Macromol Biosci. 2004; 4:743–765. [PubMed: 15468269]
2. Sharma B, Elisseeff JH. Engineering structurally organized cartilage and bone tissues. Ann Biomed Eng. 2004; 32:148–159. [PubMed: 14964730]
3. Sikavitsas VI, Temenoff JS, Mikos AG. Biomaterials and bone mechanotransduction. Biomaterials. 2001; 22:2581–2593. [PubMed: 11519777]
4. Kneser U, Schaefer DJ, Polykandriotis E, Horch RE. Tissue engineering of bone: the reconstructive surgeon's point of view. J Cell Mol Med. 2006; 10:7–19. [PubMed: 16563218]
5. Logeart-Avramoglou D, Anagnostou F, Bizios R, Petite H. Engineering bone: challenges and obstacles. J Cell Mol Med. 2005; 9:72–84. [PubMed: 15784166]

6. Jadlowiec JA, Celil AB, Hollinger JO. Bone tissue engineering: recent advances and promising therapeutic agents. Expert Opin Biol Ther. 2003; 3:409–423. [PubMed: 12783610]
7. Cancedda R, Bianchi G, Derubeis A, Quarto R. Cell therapy for bone disease: a review of current status. Stem Cells. 2003; 21:610–619. [PubMed: 12968115]
8. Langer R, Vacanti JP. Tissue engineering. Science. 1993; 260:920–926. [PubMed: 8493529]
9. Vacanti JP, Langer R. Tissue engineering: the design and fabrication of living replacement devices for surgical reconstruction and transplantation. Lancet. 1999; 354(Suppl 1):SI32–34. [PubMed: 10437854]
10. Muschler GF, Nakamoto C, Griffith LG. Engineering principles of clinical cell-based tissue engineering. J Bone Joint Surg Am. 2004; 86-A:1541–1558. [PubMed: 15252108]
11. Schantz JT, Teoh SH, Lim TC, Endres M, Lam CX, Hutmacher DW. Repair of calvarial defects with customized tissue-engineered bone grafts I. Evaluation of osteogenesis in a three-dimensional culture system. Tissue Eng. 2003; 9(Suppl 1):S113–126. [PubMed: 14511475]
12. Bajada S, Mazakova I, Richardson JB, Ashammakhi N. Updates on stem cells and their applications in regenerative medicine. J Tissue Eng Regen Med. 2008; 2:169–183. [PubMed: 18493906]
13. Deschaseaux F, Sensebe L, Heymann D. Mechanisms of bone repair and regeneration. Trends Mol Med. 2009; 15:417–429. [PubMed: 19740701]
14. Altman GH, Diaz F, Jakuba C, Calabro T, Horan RL, Chen J, Lu H, Richmond J, Kaplan DL. Silk-based biomaterials. Biomaterials. 2003; 24:401–416. [PubMed: 12423595]
15. MacIntosh AC, Kearns VR, Crawford A, Hatton PV. Skeletal tissue engineering using silk biomaterials. J Tissue Eng Regen Med. 2008; 2:71–80. [PubMed: 18383453]
16. Meinel L, Hofmann S, Karageorgiou V, Kirker-Head C, McCool J, Gronowicz G, Zichner L, Langer R, Vunjak-Novakovic G, Kaplan DL. The inflammatory responses to silk films in vitro and in vivo. Biomaterials. 2005; 26:147–155. [PubMed: 15207461]
17. Panilaitis B, Altman GH, Chen J, Jin HJ, Karageorgiou V, Kaplan DL. Macrophage responses to silk. Biomaterials. 2003; 24:3079–3085. [PubMed: 12895580]
18. Vepari C, Kaplan DL. Silk as a Biomaterial. Prog Polym Sci. 2007; 32:991–1007. [PubMed: 19543442]
19. Wang Y, Kim HJ, Vunjak-Novakovic G, Kaplan DL. Stem cell-based tissue engineering with silk biomaterials. Biomaterials. 2006; 27:6064–6082. [PubMed: 16890988]
20. Glowacki J. Engineered cartilage, bone, joints, and menisci. Potential for temporomandibular joint reconstruction. Cells Tissues Organs. 2001; 169:302–308. [PubMed: 11455127]
21. Adachi T, Osako Y, Tanaka M, Hojo M, Hollister SJ. Framework for optimal design of porous scaffold microstructure by computational simulation of bone regeneration. Biomaterials. 2006; 27:3964–3972. [PubMed: 16584771]
22. Lutolf MP, Hubbell JA. Synthetic biomaterials as instructive extracellular microenvironments for morphogenesis in tissue engineering. Nat Biotechnol. 2005; 23:47–55. [PubMed: 15637621]
23. You Z, Bi X, Fan X, Wang Y. A functional polymer designed for bone tissue engineering. Acta Biomater. 2012; 8:502–510. [PubMed: 22100348]
24. Rezwan K, Chen QZ, Blaker JJ, Boccaccini AR. Biodegradable and bioactive porous polymer/inorganic composite scaffolds for bone tissue engineering. Biomaterials. 2006; 27:3413–3431. [PubMed: 16504284]
25. Horan RL, Antle K, Collette AL, Wang Y, Huang J, Moreau JE, Volloch V, Kaplan DL, Altman GH. In vitro degradation of silk fibroin. Biomaterials. 2005; 26:3385–3393. [PubMed: 15621227]
26. Cunniff PM, Fossey SA, Auerbach MA, Song JW, Kaplan DJ, Adams WW, Eby RK, Mahoney D, Vezie DL. Mechanical and thermal properties of the dragline silk from the spider Nephila claviceps. Poly Adv Technol. 1994; 5:401–410.
27. Jin HJ, Chen J, Karageorgiou V, Altman GH, Kaplan DL. Human bone marrow stromal cell responses on electrospun silk fibroin mats. Biomaterials. 2004; 25:1039–1047. [PubMed: 14615169]

28. Hofmann S, Hagenmüller H, Koch AM, Müller R, Vunjak-Novakovic G, Kaplan DL, Merkle HP, Meinel L. Control of in vitro tissue-engineered bone-like structures using human mesenchymal stem cells and porous silk scaffolds. Biomaterials. 2007; 28:1152–1162. [PubMed: 17092555]
29. Uebersax L, Hagenmuller H, Hofmann S, Gruenblatt E, Muller R, Vunjak-Novakovic G, Kaplan DL, Merkle HP, Meinel L. Effect of scaffold design on bone morphology in vitro. Tissue Eng. 2006; 12:3417–3429. [PubMed: 17518678]
30. Karageorgiou V, Kaplan D. Porosity of 3D biomaterial scaffolds and osteogenesis. Biomaterials. 2005; 26:5474–5491. [PubMed: 15860204]
31. Kasten P, Beyen I, Niemeyer P, Luginbuhl R, Bohner M, Richter W. Porosity and pore size of beta-tricalcium phosphate scaffold can influence protein production and osteogenic differentiation of human mesenchymal stem cells: an in vitro and in vivo study. Acta Biomater. 2008; 4:1904–1915. [PubMed: 18571999]
32. Tsigkou O, Pomerantseva I, Spencer JA, Redondo PA, Hart AR, O'Doherty E, Lin Y, Friedrich CC, Daheron L, Lin CP, Sundback CA, Vacanti JP, Neville C. Engineered vascularized bone grafts. Proc Natl Acad Sci U S A. 2010; 107:3311–3316. [PubMed: 20133604]
33. von Doernberg MC, von Rechenberg B, Bohner M, Grunenfelder S, van Lenthe GH, Muller R, Gasser B, Mathys R, Baroud G, Auer J. In vivo behavior of calcium phosphate scaffolds with four different pore sizes. Biomaterials. 2006; 27:5186–5198. [PubMed: 16790273]
34. Nazarov R, Jin HJ, Kaplan DL. Porous 3-D scaffolds from regenerated silk fibroin. Biomacromolecules. 2004; 5:718–726. [PubMed: 15132652]
35. Sofia S, McCarthy MB, Gronowicz G, Kaplan DL. Functionalized silk-based biomaterials for bone formation. J Biomed Mater Res. 2001; 54:139–148. [PubMed: 11077413]
36. Meinel L, Hofmann S, Karageorgiou V, Zichner L, Langer R, Kaplan D, Vunjak-Novakovic G. Engineering cartilage-like tissue using human mesenchymal stem cells and silk protein scaffolds. Biotechnol Bioeng. 2004; 88:379–391. [PubMed: 15486944]
37. Meinel L, Karageorgiou V, Fajardo R, Snyder B, Shinde-Patil V, Zichner L, Kaplan D, Langer R, Vunjak-Novakovic G. Bone tissue engineering using human mesenchymal stem cells: effects of scaffold material and medium flow. Ann Biomed Eng. 2004; 32:112–122. [PubMed: 14964727]
38. Meinel L, Karageorgiou V, Hofmann S, Fajardo R, Snyder B, Li C, Zichner L, Langer R, Vunjak-Novakovic G, Kaplan DL. Engineering bone-like tissue in vitro using human bone marrow stem cells and silk scaffolds. J Biomed Mater Res A. 2004; 71:25–34. [PubMed: 15316936]
39. Rüegsegger P, Koller B, Müller R. A microtomographic system for the nondestructive evaluation of bone architecture. Calcif Tissue Int. 1996; 58:24–29. [PubMed: 8825235]
40. Hildebrand T, Laib A, Müller R, Dequeker J, Rüegsegger P. Direct three-dimensional morphometric analysis of human cancellous bone: microstructural data from spine, femur, iliac crest, and calcaneus. J Bone Miner Res. 1999; 14:1167–1174. [PubMed: 10404017]
41. Müller R, Hildebrand T, Rüegsegger P. Non-invasive bone biopsy: a new method to analyse and display the three-dimensional structure of trabecular bone. Phys Med Biol. 1994; 39:145–164. [PubMed: 7651993]
42. Kim KH, Jeong L, Park HN, Shin SY, Park WH, Lee SC, Kim TI, Park YJ, Seol YJ, Lee YM, Ku Y, Rhyu IC, Han SB, Chung CP. Biological efficacy of silk fibroin nanofiber membranes for guided bone regeneration. J Biotechnol. 2005; 120:327–339. [PubMed: 16150508]
43. Fini M, Motta A, Torricelli P, Giavaresi G, Nicoli Aldini N, Tschon M, Giardino R, Migliaresi C. The healing of confined critical size cancellous defects in the presence of silk fibroin hydrogel. Biomaterials. 2005; 26:3527–3536. [PubMed: 15621243]
44. Meinel L, Hofmann S, Betz O, Fajardo R, Merkle HP, Langer R, Evans CH, Vunjak-Novakovic G, Kaplan DL. Osteogenesis by human mesenchymal stem cells cultured on silk biomaterials: comparison of adenovirus mediated gene transfer and protein delivery of BMP-2. Biomaterials. 2006; 27:4993–5002. [PubMed: 16765437]
45. Radin EL, Rose RM. Role of subchondral bone in the initiation and progression of cartilage damage. Clin Orthop Relat Res. 1986:34–40. [PubMed: 3780104]
46. Meinel L, Fajardo R, Hofmann S, Langer R, Chen J, Snyder B, Vunjak-Novakovic G, Kaplan D. Silk implants for the healing of critical size bone defects. Bone. 2005; 37:688–698. [PubMed: 16140599]

47. Meinel L, Betz O, Fajardo R, Hofmann S, Nazarian A, Cory E, Hilbe M, McCool J, Langer R, Vunjak-Novakovic G, Merkle HP, Rechenberg B, Kaplan DL, Kirker-Head C. Silk based biomaterials to heal critical sized femur defects. Bone. 2006; 39:922–931. [PubMed: 16757219]
48. Kirker-Head C, Karageorgiou V, Hofmann S, Fajardo R, Betz O, Merkle HP, Hilbe M, von Rechenberg B, McCool J, Abrahamsen L, Nazarian A, Cory E, Curtis M, Kaplan D, Meinel L. BMP-silk composite matrices heal critically sized femoral defects. Bone. 2007; 41:247–255. [PubMed: 17553763]
49. Schantz JT, Hutmacher DW, Lam CX, Brinkmann M, Wong KM, Lim TC, Chou N, Guldberg RE, Teoh SH. Repair of calvarial defects with customised tissue-engineered bone grafts II. Evaluation of cellular efficiency and efficacy in vivo. Tissue Eng. 2003; 9(Suppl 1):S127–139. [PubMed: 14511476]
50. Meyer U, Neunzehn J, Wiesmann HP. Computer-aided approach for customized cell-based defect reconstruction. Methods Mol Biol. 2012; 868:27–43. [PubMed: 22692602]
51. Sicchieri LG, Crippa GE, de Oliveira PT, Beloti MM, Rosa AL. Pore size regulates cell and tissue interactions with PLGA-CaP scaffolds used for bone engineering. J Tissue Eng Regen Med. 2012; 6:155–162. [PubMed: 21446054]
52. Karageorgiou V, Kaplan D. Porosity of 3D biomaterial scaffolds and osteogenesis. Biomaterials. 2005; 26:5474–5491. [PubMed: 15860204]
53. Kuboki Y, Takita H, Kobayashi D, Tsuruga E, Inoue M, Murata M, Nagai N, Dohi Y, Ohgushi H. BMP-induced osteogenesis on the surface of hydroxyapatite with geometrically feasible and nonfeasible structures: topology of osteogenesis. J Biomed Mater Res. 1998; 39:190–199. [PubMed: 9457547]
54. Cadet ER, Gafni RI, McCarthy EF, McCray DR, Bacher JD, Barnes KM, Baron J. Mechanisms responsible for longitudinal growth of the cortex: coalescence of trabecular bone into cortical bone. J Bone Joint Surg Am. 2003; 85-A:1739–1748. [PubMed: 12954833]
55. Bohner M, Loosli Y, Baroud G, Lacroix D. Commentary: Deciphering the link between architecture and biological response of a bone graft substitute. Acta Biomater. 2010
56. Jasty, M. Bone graft and bone substitutes. Habal, M.; Reddi, A., editors. Saunders; London: 1992. p. 399
57. Caplan AI. Mesenchymal stem cells. J Orthop Res. 1991; 9:641–650. [PubMed: 1870029]
58. Volkmer E, Drosse I, Otto S, Stangelmayer A, Stengele M, Kallukalam BC, Mutschler W, Schieker M. Hypoxia in static and dynamic 3D culture systems for tissue engineering of bone. Tissue Eng Part A. 2008; 14:1331–1340. [PubMed: 18601588]
59. Mastrogiacomo M, Scaglione S, Martinetti R, Dolcini L, Beltrame F, Cancedda R, Quarto R. Role of scaffold internal structure on in vivo bone formation in macroporous calcium phosphate bioceramics. Biomaterials. 2006; 27:3230–3237. [PubMed: 16488007]
60. Sims, N.; Baron, R. Bone Cells and Their Functions. In: Canalis, E., editor. Skeletal Growth Factors. Lippincott Williams & Wilkins; Philadelphia: 2000. p. 1-17.
61. Kuboki Y, Jin Q, Kikuchi M, Mamood J, Takita H. Geometry of artificial ECM: sizes of pores controlling phenotype expression in BMP-induced osteogenesis and chondrogenesis. Connect Tissue Res. 2002; 43:529–534. [PubMed: 12489210]
62. Wray LS, Hu X, Gallego J, Georgakoudi I, Omenetto FG, Schmidt D, Kaplan DL. Effect of processing on silk-based biomaterials: Reproducibility and biocompatibility. J Biomed Mater Res B Appl Biomater. 2011
63. Lickorish D, Chan J, Song J, Davies JE. An in-vivo model to interrogate the transition from acute to chronic inflammation. Eur Cell Mater. 2004; 8:12–19. discussion 20. [PubMed: 15494930]
64. Brandl F, Sommer F, Goepferich A. Rational design of hydrogels for tissue engineering: impact of physical factors on cell behavior. Biomaterials. 2007; 28:134–146. [PubMed: 17011028]

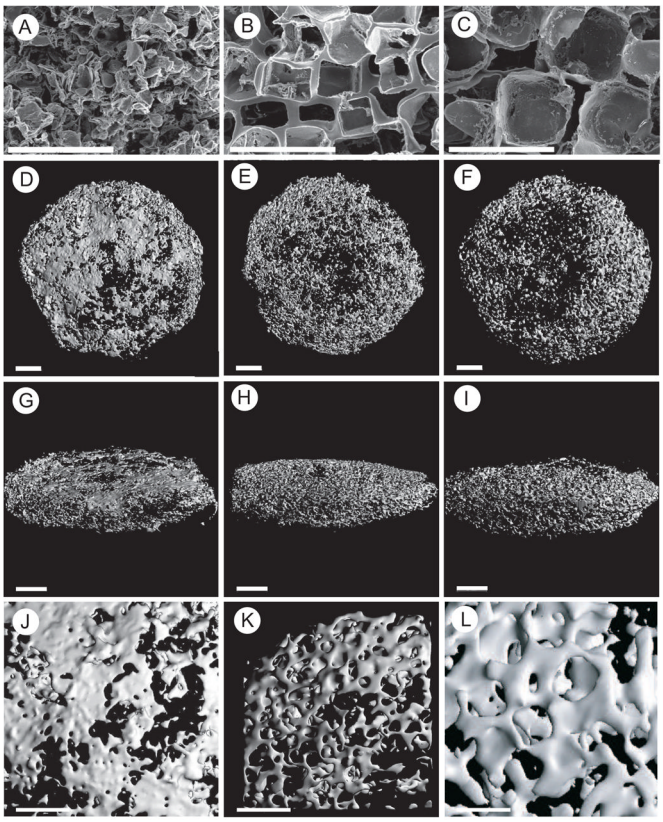

Figure 1.

SEM images (A–C) of silk fibroin scaffolds decorated with RGD sequences with small (106–212 μm), medium (212–300 μm) or large (300–425 μm) pore diameters. Micro-CT images (D–L) taken from the same scaffolds seeded with hMSC after 5 weeks of cultivation under osteogenic conditions in spinner flasks, showing the constructs as seen from the top (D–F), from the side (G–I) and higher magnification (J–L). Bar length: 500 μm (A–C), 2 mm (D–I), 1 mm (J–L).

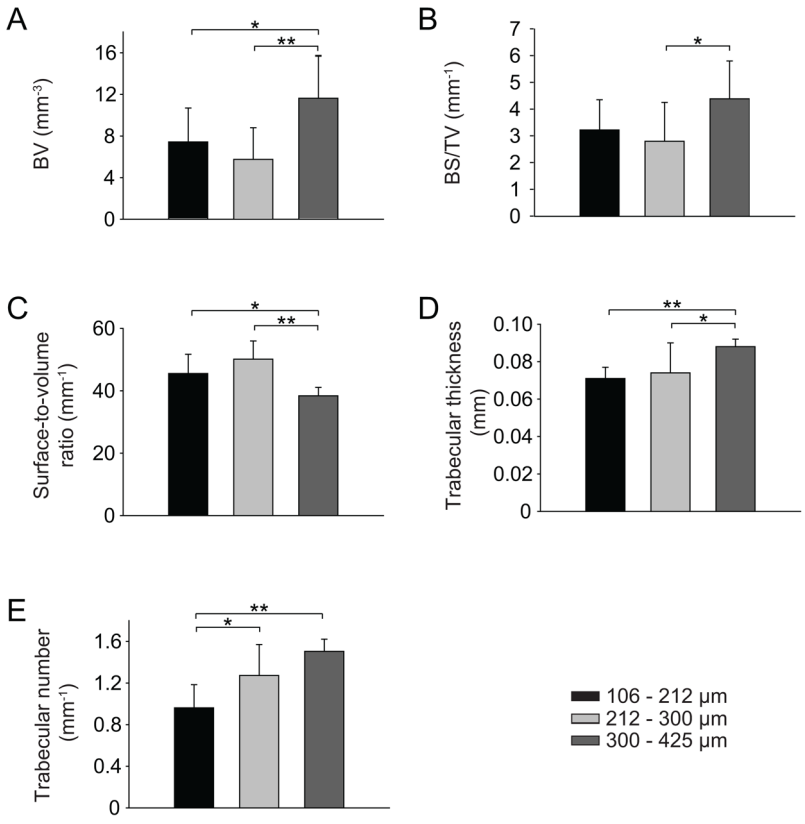

Figure 2.

Histomorphometrical analysis of tissue-engineered bone-like structures formed by hMSC seeded on silk-RGD scaffolds with small (106–212 μm), medium (212–300 μm) or large (300–425 μm) pore diameters under osteogenic conditions in spinner flask bioreactors after 5 weeks of in vitro culture. Bone volume (A), bone surface per total volume (B), bone surface-to-volume ratio (C), trabecular thickness (D) and trabecular number (E). * Significant difference at $p < 0.05$, ** significant difference at $p < 0.01$.

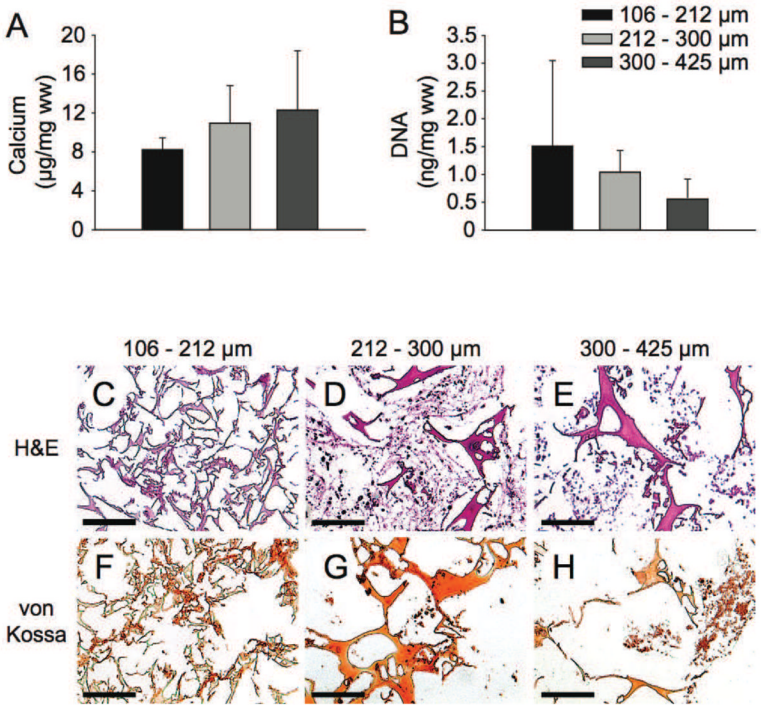

Figure 3.

Biochemical and histological analysis of tissue-engineered bone-like structures formed by hMSC seeded on silk fibroin scaffolds decorated with RGD sequences with small (106–212 μm), medium (212–300 μm) or large (300–425 μm) pore diameters, respectively, under osteogenic conditions in spinner flask bioreactors after 5 weeks of in vitro culture. (A) Calcium deposition per scaffold wet weight and (B) DNA per scaffold wet weight, (C–E) sections stained with H&E, (F–H) sections stained with von Kossa. * Significant difference at $p < 0.05$, ** significant difference at $p < 0.01$; bar length 100 μm.

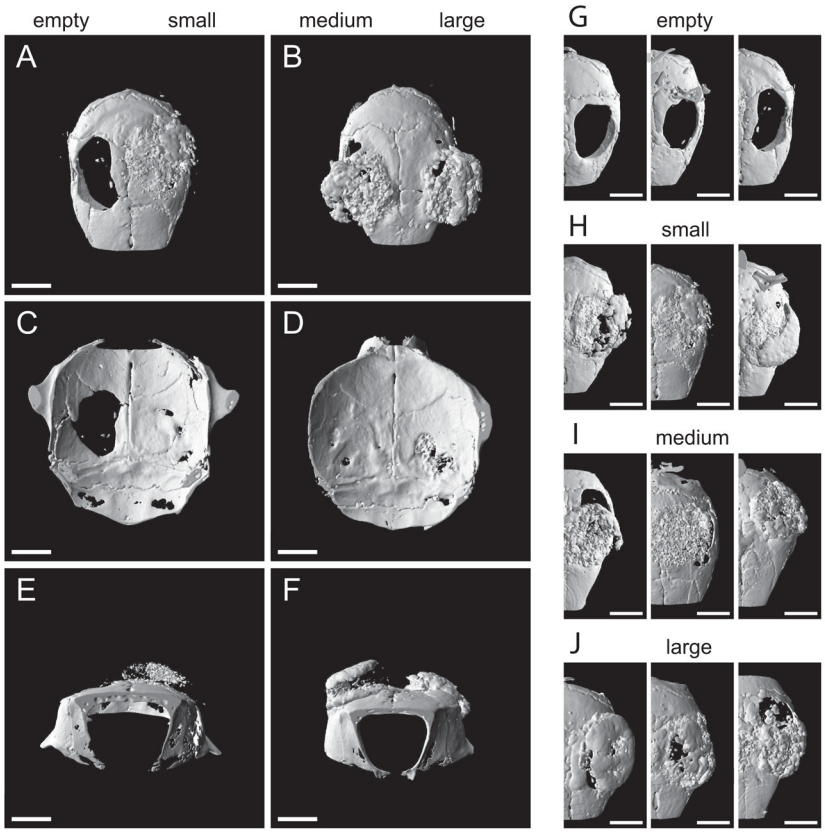

Figure 4.

Representative micro-computed tomography images of mouse calvarial defects 8 weeks after surgery. Defects were left empty (A, C, E: left side; G) or were treated with implants made of tissue-engineered bone on silk fibroin scaffolds decorated with RGD sequences with a small (106–212 μm) pore diameter (A, C, E: right side; H), a medium (212–300 μm) pore diameter (B, D, F: left side: I) or a large (300–425 μm) pore diameter (B, D, F: right side; J). Apical views (A, B, G, H, I, J), caudal views (C, D) or front views (E, F). Bar length is 2 mm.

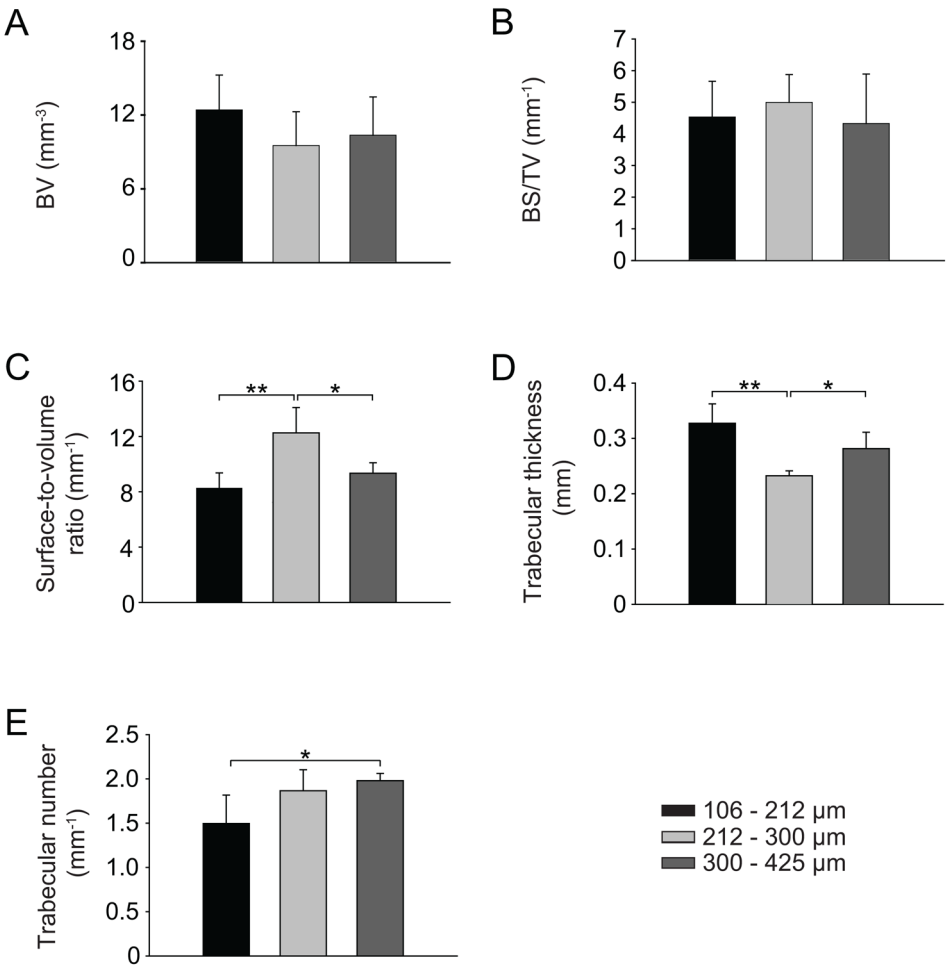

Figure 5.

Histomorphometrical analysis of mouse calvarial defects 8 weeks after surgery. Bone volume (A), bone surface per total volume (B), bone surface-to-volume ratio (C), trabecular thickness (D), and trabecular number (E). * Significant difference at $p < 0.05$, ** significant difference at $p < 0.01$.

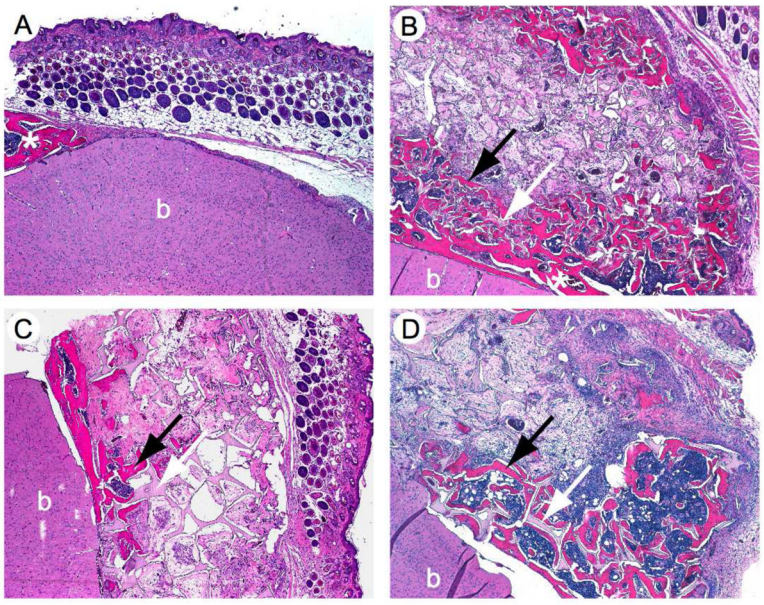

Figure 6.

Histological sections of mouse calvarial defects 8 weeks after surgery and stained with H&E. Defects were left empty (A) or were treated with implants made of tissue-engineered bone on silk fibroin scaffolds decorated with RGD sequences with a small (106–212 μm) average pore diameter (B), a medium (212–300 μm) average pore diameter (C) or a large (300–425 μm) average pore diameter (D). b = brain tissue, white arrow = silk scaffold, black arrow = newly formed bone, * = host bone. Magnification 4x

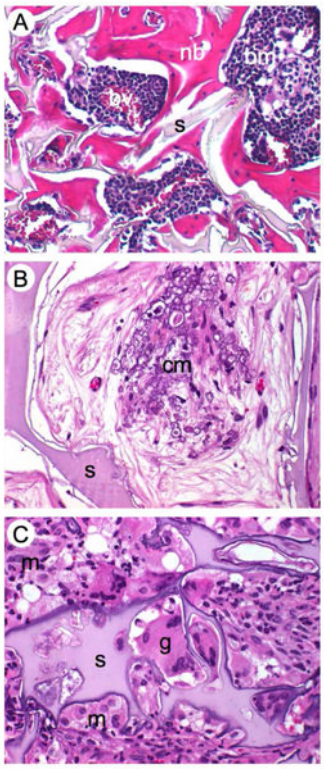

Figure 7.
Histological details of mouse calvarial defects 8 weeks after surgery and stained with H&E. (A) Newly formed bone around the silk fibroin scaffold decorated with RGD sequences showing normal bone morphology, bone marrow and vascularization. (B) Clusters of beginning mineralization in the pore void, (C) silk with mineralizing edges surrounded by foreign body giant cells, neutrophils and macrophages that start degrading the silk-RGD. nb = newly formed bone, s = silk, bm = bone marrow, bv = blood vessels, cm = clusters of mineralization, g = giant cell, m = macrophage, n = neutrophil. Magnification 40x

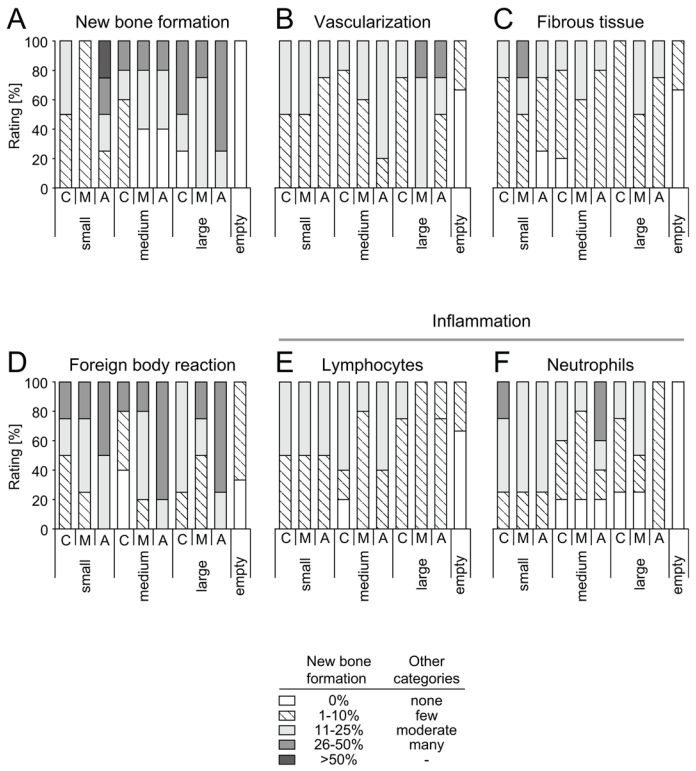

Figure 8.

Semiquantitative analysis of histological images showing new bone formation, vascularization, fibrous tissue, foreign body reaction as well as lymphocyte and neutrophil granulocyte numbers 8 weeks after surgery. Values are ratings in percent of defects analysed for small (106–212 μm), medium (212–300 μm) or large (300–425 μm) pore diameter of scaffolds that were divided into a caudal (C), middle (M) and apical (A) part.